MIT Open Access Articles

Parallel transport studies of high-Z impurities in the core of Alcator C-Mod plasmas

Massachusetts Institute of Technology

M. L. Reinke, I. H. Hutchinson, J. E. Rice, M. Greenwald, N. T. Howard, A. Hubbard, J. W. Hughes, J. L. Terry, and S. M. Wolfe
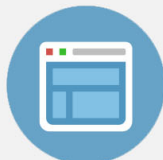
Parallel transport studies of high-Z impurities in the core of Alcator C-Mod plasmas[a]

M. L. Reinke,[b] I. H. Hutchinson, J. E. Rice, M. Greenwald, N. T. Howard, A. Hubbard, J. W. Hughes, J. L. Terry, and S. M. Wolfe

MIT-Plasma Science and Fusion Center Cambridge, Massachusetts 02139, USA

Measurements of poloidal variation, $\tilde{n}_z/\langle n_z \rangle$, in high-Z impurity density have been made using photodiode arrays sensitive to vacuum ultraviolet and soft x-ray emission in Alcator C-Mod plasmas. In/out asymmetries in the range of $-0.2 < n_{z,cos}/\langle n_z \rangle < 0.3$ are observed for $r/a < 0.8$, and accumulation on both the high-field side, $n_{z,cos} < 0$, and low-field side, $n_{z,cos} > 0$, of a flux surface is found to be well described by a combination of centrifugal, poloidal electric field, and ion-impurity friction effects. Up/down asymmetries, $-0.05 < n_{z,sin}/\langle n_z \rangle < 0.10$, are observed over $0.5 < r/a < 0.9$ with $n_{z,sin} > 0$ corresponding to accumulation opposite the ion ∇B drift direction. Measurements of the up/down asymmetry of molybdenum are found to disagree with predictions from recent neoclassical theory in the trace limit, $n_z Z^2/n_i \ll 1$. Non-trace levels of impurities are expected to modify the main-ion poloidal flow and thus change friction-driven impurity density asymmetries and impurity poloidal rotation, $v_{\theta,z}$. Artificially modifying main-ion flow in parallel transport simulations is shown to impact both $\tilde{n}_z/\langle n_z \rangle$ and $v_{\theta,z}$, but simultaneous agreement between measured and predicted up/down and in/out asymmetry as well as impurity poloidal rotation is not possible for these C-Mod data. This link between poloidal flow and poloidal impurity density variation outlines a more stringent test for parallel neoclassical transport theory than has previously been performed. Measurement and computational techniques specific to the study of poloidal impurity asymmetry physics are discussed as well. © *2013 AIP Publishing LLC.*
[http://dx.doi.org/10.1063/1.4802197]

I. INTRODUCTION

Often it is assumed, sometimes incorrectly, that transport along the magnetic field is strong enough to make the density and temperature of all species flux-functions to first order in $\delta = \rho/L$, the ion gyroradius normalized the radial scale length, which is $\ll 1$ over most of the plasma volume. But, as has been pointed out by several authors,[1–10] it is possible to sustain gradients in impurity pressure along the field, even while retaining the nominal flux-surface symmetry of the main-ion and electron species. Recent theoretical work suggests that such poloidal variations of high-Z impurity density can have a large impact on their turbulence-driven, flux-surface averaged radial transport,[11,12] increasing the importance of a fully validated theory for $n_z(\theta)$. Additionally, strong poloidal asymmetries can lead to misinterpretation of diagnostic measurements if they are collected over a limited range of poloidal angles. In such instances, a thorough understanding of impurity asymmetry physics could avoid this systematic error using additional observations of the background plasma.

Although the basic parallel momentum balance equations are the same for ions and impurities, the charge and mass of the impurities weight terms differently. The larger impurity mass enhances inertial effects like the centrifugal force,[1,4,5] tending to move impurities to the low-field side (LFS) of a flux surface, even in cases of intrinsic toroidal rotation. The high charge of the impurity amplifies any small poloidal variation of the electrostatic potential and the impurities respond in a Boltzmann-like manner to $\Phi(\theta)$ along the field.[10,13] When the impurity density is small, $n_z Z^2/n_i \ll 1$, self-collisions are negligible and collisional processes with the main-ion species dominate, and may lead to an impurity density asymmetry that is driven by the poloidally varying ion-impurity friction.[2,3,6,8,9]

Many of these effects have been observed on tokamaks, but a comprehensive validation of neoclassical parallel impurity transport has not previously been completed. The effect of the centrifugal force was first seen on ASDEX[14] and was quantitatively investigated on JET.[15] The impact of poloidal electric fields driven by ion cyclotron resonance heating (ICRH) was first seen on JET,[13] while recent work on C-Mod[10] has demonstrated agreement with theory for the combined effects of inertia and electrostatic forces. The present research focuses on more complete validation of parallel transport of high-Z impurities, examining both up/down and in/out asymmetries driven by inertia, electrostatic and friction forces. In this work, in/out asymmetries of molybdenum are found to be in good agreement in the core, $r/a < 0.8$, of C-Mod plasmas, while up/down asymmetries are much smaller magnitude than predicted for H-mode plasmas. Changes in main-ion poloidal rotation are shown to impact both impurity asymmetries and impurity poloidal rotation, demonstrating a link between both flow and asymmetry physics and describing a much more stringent test for future validation efforts in parallel ion transport.

In this paper, Sec. II describes the background on the neoclassical parallel impurity theory thought to describe $n_z(\theta)$. Section III illustrates the diagnostic and analysis tools developed specifically to study both in/out and up/down asymmetries in high-Z emission. Section IV presents measurements of the 2D structure of molybdenum density on Alcator C-Mod in ion cyclotron range of frequency (ICRF) heated H-mode plasmas, demonstrating good predictions for in/out asymmetries but large discrepancies for up/down asymmetries, and Sec. V investigates the role of main-ion poloidal flow in determining the poloidal density variation. This paper strives to summarize and highlight the wide range of C-Mod observations discussed in substantial detail in Ref. 16.

II. PRIOR WORK ON NEOCLASSICAL PARALLEL IMPURITY TRANSPORT

To determine the poloidal variation of the impurity density, their source free, steady-state particle conservation (1), and momentum balance (2) equations are used. Due to their higher charge and mass, impurities are generally assumed to be in the collisional regime, and the fluid equations for the impurities are employed nearly universally in analytical theory.

$$\nabla \cdot (n_z \mathbf{V}_z) = 0, \tag{1}$$

$$n_Z m_Z (\mathbf{V}_z \cdot \nabla) \mathbf{V}_z + \nabla p_z + \nabla \cdot \pi_z + Z n_z \nabla \Phi$$
$$+ Z n_z (\mathbf{V}_z \times \mathbf{B}) = \mathbf{F_z}, \tag{2}$$

where $\mathbf{F}_z$ is the sum of the friction forces and π_z is the viscosity tensor. Here, $\mathbf{V}_z$ is the mean flow of the impurity. In toroidal geometry, divergence free flow for any ion species, a, gives

$$\mathbf{V}_a = -\left(\frac{\partial \Phi}{\partial \psi} + \frac{1}{Z_a e n_a}\frac{\partial p_a}{\partial \psi}\right) R\hat{\phi} + \frac{K_a}{n_a}\mathbf{B}, \tag{3}$$

where K_a is an arbitrary flux-function.[17] An axisymmetric magnetic field, $\vec{B} = I(\psi)\nabla\phi + \nabla\psi \times \nabla\phi$, is assumed.

The energy conservation can generally be ignored as the impurity-ion energy equilibration timescale, τ_{zi}^E, is significantly less than the impurity parallel momentum equilibration timescale, $\tau_{\|,z}$, making $T_z = T_i$, with $\tilde{T}_i/\langle T_i\rangle \ll 1$.[6] In order to decouple the parallel and perpendicular transport, allowing the parallel transport to be solved first, independently of the cross-field transport, $\tau_{\|,z} \ll \tau_{\perp,z}$ is required, in agreement with neoclassical theory.[6] The anomalous radial transport works to decrease $\tau_{\perp,z}$, but using impurity transport simulations to estimate the diffusion and convection[18] shows $\tau_{\|,z} \ll \tau_{\perp,z}$ is still well satisfied in the core of C-Mod plasmas discussed here. In colder regions, near the edge of L-mode plasmas, this assumption begins to be violated as parallel impurity diffusivity becomes small, and the impact on parallel impurity transport is discussed in Ref. 19. The viscous force has been shown to be weak relative to the friction force[6] and solid body toroidal rotation, ω, will dominate the inertial term. This reduces the parallel impurity transport problem to finding solutions to

$$\frac{m_z n_z \omega^2}{2}\nabla_\| R^2 + Z n_z e \nabla_\| \Phi + T_z \nabla_\| n_z = F_{z,\|}. \tag{4}$$

The importance of rotation in driving impurity asymmetries via inertia is well known with Ref. 1 deriving the first expression for $n_z(\theta)$, a result also discussed in Refs. 4 and 5. The first experimental observation of the inertia driving an in/out impurity emission asymmetry was seen on ASDEX.[14] More recently an in/out asymmetry in soft X-ray (SXR) emission was observed in ASDEX-Upgrade neutral beam heated ELMy H-mode discharges seeded with Kr.[20] JET has also used SXR tomography to investigate in/out asymmetries in impurity emission during beam-heated ELM-free[21] and hot-ion H-modes,[22] as well as in optimized shear (OS) plasmas[15,23] where measured asymmetries were found to quantitatively agree with analytical predictions.

The impact of ion-impurity friction on parallel impurity transport was first discussed in Refs. 2 and 3 focusing on the drive for an up/down asymmetry. In cases of strong ion-impurity friction, an in/out asymmetry, with a build-up of impurities on the high-field side (HFS), was first outlined in Ref. 24 with Ref. 25 describing this in more detail for a circular, collisional, isothermal plasma. That work was extended to include ion temperature gradients and describe the banana,[6] Pfirsch-Schlüter[8] and plateau[9] regimes.

The first observation of the up/down asymmetry was seen on Alcator-A[26] using poloidally scanning vacuum ultraviolet (VUV) spectroscopy to measure brightness profiles of O VI and O V line emission above and below the midplane. The brightness was observed to be higher on the side away from the ion ∇B drift direction and was larger at higher densities in qualitative agreement with predictions in Ref. 2. Similar measurements on PLT[27] demonstrated the asymmetry did not change when the ∇B direction was reversed, but instead was observed to be correlated to the position of the limiter and increased with higher edge temperature. The conclusion was that localized plasma-wall interaction was creating a poloidally localized impurity source that was not yet symmeterized for low ionization states. The comparison of the Alcator-A and PLT results demonstrates the difficulty of interpreting measured asymmetries near the edge of the plasma, $r/a > 0.8$, due to the sensitivity to both localized sources and neoclassical transport. Up/down emission asymmetries attributed to ion-impurity friction have since been widely observed in PDX,[3] COMPASS-C,[28] TEXT,[29] Phaedrus-T,[30] JET,[31] and Alcator C-Mod.[32] Both PDX and JET measured asymmetries in carbon and showed good agreement to existing theory, while measurements of up/down asymmetries in argon on C-Mod showed strong disagreements. More recently, an in/out asymmetry in low-Z emission in the pedestal of H-mode plasmas has been inferred from charge exchange measurements on C-Mod[33,34] and AUG,[35] possibly due to strong friction in the steep-gradient region of the edge transport barrier.

A. Comprehensive parallel impurity transport theory

Few attempts have been made to solve the full parallel force balance equation including both friction and inertial

forces (4) in the banana regime which describes high-Z impurities in the core of C-Mod and other fusion-grade plasmas. In both Refs. 25 and 36, friction and inertia were combined but only assumed collisional main-ions, with Ref. 36 oversimplifying the ion-impurity friction. The first combination of friction and inertia in the banana regime was shown in Ref. 37, deriving relations for both the in/out and up/down asymmetries assuming a small inverse aspect ratio and circular geometry. Similar work was developed in Ref. 38 which also included viscosity along with inertia and friction forces, although the poloidal ion flow was not constrained using neoclassical theory and was left to be specified empirically. In both cases, poloidal electric field effects were ignored: estimating, correctly, that $e\tilde{\phi}/T_e$ is small, but failing to realize that $Ze\tilde{\phi}/T_e$ is what enters into the impurity force balance and can be of order unity. As shown in Ref. 4, this is not only an important piece of the asymmetry driven by the centrifugal force but can also be sustained by magnetically trapped non-thermal particles which occur during ICRF heating[10,13] or with radial neutral beams.[39]

In Ref. 7, the 1D parallel transport equation was derived for banana regime main-ions and fluid, high-Z impurities including both inertia and friction. This has been judged to be, at present, the most complete neoclassical parallel impurity transport for comparing to experimental C-Mod results, and forms the basis of numerical simulations as discussed in Sec. II B. In the trace limit, $n_z Z^2/n_i \ll 1$, Eq. (4) reduces to

$$\frac{\partial n}{\partial \vartheta} = g\left[n + \gamma\left(n - \frac{K_z}{\langle n_z\rangle u_i}\right)b^2\right] + \frac{\partial M^2}{\partial \vartheta}n, \qquad (5)$$

where $n = n_z/\langle n_z\rangle$, $d\vartheta/d\theta \equiv \langle\vec{B}\cdot\nabla\theta\rangle/\vec{B}\cdot\nabla\theta$, and $b^2 = B^2/\langle B^2\rangle$. The coefficients in this 1D differential equation are included below for completeness, with interested readers directed to Ref. 7 for details regarding the derivation of Eq. (5). The M^2, g, γ, and u_i terms, respectively, are

$$M^2 = \frac{m_z \omega^2 R^2}{2 T_z}\left(1 - \frac{Z m_i}{m_z}\frac{T_e}{T_e + T_i}\right), \qquad (6)$$

$$g = -\frac{m_i Z^2 I}{e\tau_{ii}\langle\mathbf{B}\cdot\nabla\theta\rangle}\left(\frac{1}{n_i}\frac{\partial n_i}{\partial \psi} - \frac{1}{2}\frac{1}{T_i}\frac{\partial T_i}{\partial \psi}\right), \qquad (7)$$

$$\gamma g = -\frac{m_i Z^2 I f_c}{3 e\tau_{ii}\langle\mathbf{B}\cdot\nabla\theta\rangle}\frac{1}{T_i}\frac{\partial T_i}{\partial \psi}, \qquad (8)$$

$$u_i = -\frac{I f_c}{3 e\langle B^2\rangle}\frac{\partial T_i}{\partial \psi}, \qquad (9)$$

where f_c is the fraction of circulating ions and the product of g and γ specified in Eq. (8) for clarity. Note that this value of γg is for the trace limit, and u_i assumes $r/R_o \ll 1$, while more general expressions can be found in Ref. 7. The arbitrary flux-surface constant, K_z, is found by solving Eq. (5) with a periodic boundary condition, $n(0) = n(2\pi)$, and is what determines the field-aligned flow in Eq. (3).

Assumptions of small inverse-aspect ratio, circular flux-surfaces may be used to simplify (5) to find the lowest order

in/out (n_c) and up/down (n_s) impurity asymmetries, where $n = 1 + n_c\cos\theta + n_s\sin\theta$ and

$$n_c = 2\frac{r}{R_o}\frac{M_0^2 - (1+\gamma)g^2}{1 + (1+\gamma)^2 g^2}, \qquad (10)$$

$$n_s = 2g\frac{r}{R_o}\frac{1 + (1+\gamma)M_0^2}{1 + (1+\gamma)^2 g^2} \qquad (11)$$

with $M_0^2 = M^2 R_o^2/R^2$.[7] These are referred to as the $m = 1$ or circular limit asymmetries and capture the basic physics. For modest ion-impurity friction driven by differences in diamagnetic flow, $g \simeq 1$, there exists a small up/down asymmetry with some reduction to the inertially driven low-field side accumulation, $n_c > 0$. For substantial friction, $g \gg 1$, the in/out asymmetry saturates with strong high-field accumulation, $n_c < 0$, with the up/down asymmetry dropping as $1/g$. The friction driven by purely poloidal flow, γg, can modify this picture, but in the banana regime it is generally weak with $\gamma g < 0.1$.

B. Computing the expected asymmetry

For asymmetries driven purely by friction, centrifugal or a mix of centrifugal and ICRH-driven poloidal fields, there exist analytical expressions for the poloidal impurity density variation within a flux surface, $n_z(\theta)/n_z(\theta = 0)$. For enhanced D-$\alpha$ (EDA) H-mode plasmas investigated on C-Mod, all are important, requiring a more general approach. Additionally, theories are derived in the circular limit, where the poloidally varying terms are expanded using a low-order Fourier series. Experiments use shaped plasmas where parallel derivatives cannot be computed analytically and the 1D inhomogeneous linear differential equation for $n_z(\theta)/\langle n_z\rangle$ must be solved numerically using the experimental flux-surface geometry and measurements of the relevant radial profiles.

A code written in Interactive Data Language (IDL) to solve (5) is described in detail in the Appendix. In Figure 1, example outputs of this code are shown for molybdenum in C-Mod-like plasmas, with further description of the inputs also included in the Appendix. The radial profiles are defined to highlight a combination of both centrifugal and ion-impurity friction effects which drive both in/out and up/down asymmetries. Figure 1(a) displays the numerical solution (black) for the poloidal density variation at large minor radius where friction is strong and plasma shaping leads to differences between the numerical result and the circular expansion (blue dashed). For these conditions, the solution is far from the analytical limit of only centrifugal force (red dashed-dotted) or ion-impurity friction (green dotted). Figure 1(b) shows the radial profile of the in/out and up/down asymmetry computed from this result which will be compared to C-Mod experiments. For the in/out this is defined to be $[n(0) - n(\pi)]/[n(0) + n(\pi)]$ while for the up/down $[n(\pi/2) - n(3\pi/2)]/[n(\pi/2) + n(3\pi/2)]$ is used. As shown in both plots in Figure 1(b), the analytical $m = 1$ expansion agrees very well with the $m = 1$ term computed from the full numerical solution in a shaped plasma.

Experimental inputs to this code are provided using Thomson scattering for n_e and T_e with additional electron
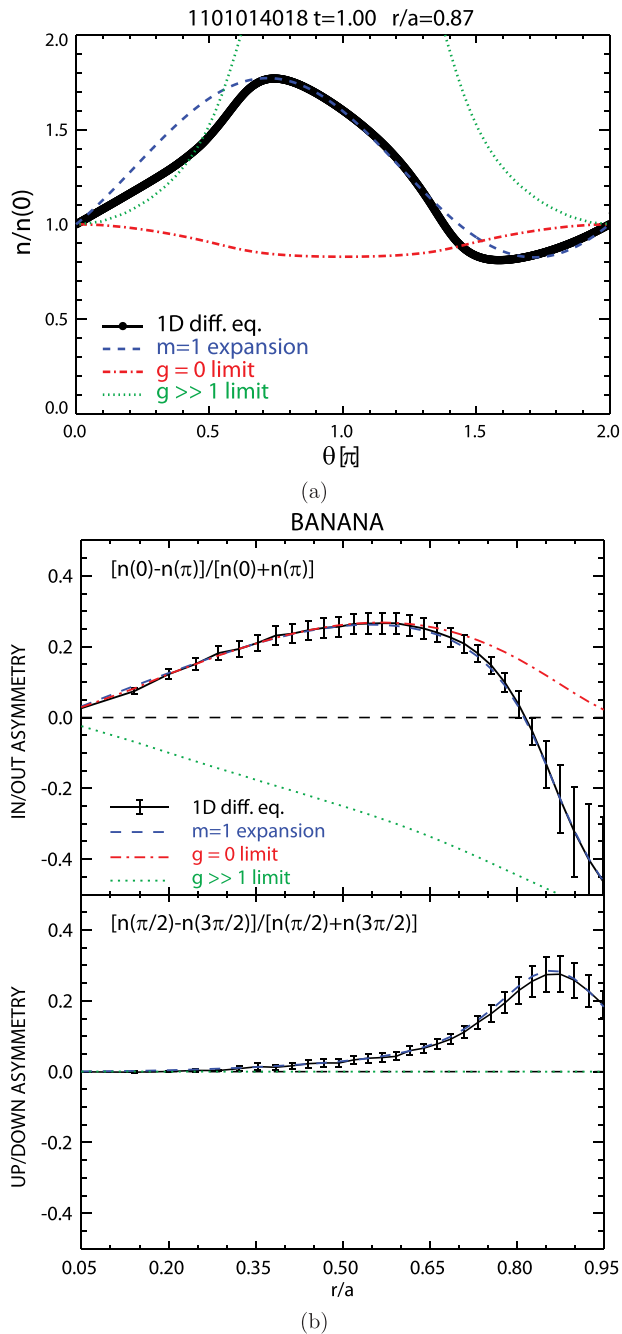
FIG. 1. Verification of parallel impurity force balance code (see Appendix) against analytical theory. In (a), computed variation within a flux surface (black) agrees well with theory using low-order Fourier exansion (blue). Radial profiles of in/out and up/down asymmetries also show excellent agreement (b).

temperature measurements from electron cyclotron emission.[40] Impurity flow and temperature measurements are found using x-ray imaging crystal spectroscopy (XICS).[41,42]

III. DIAGNOSTIC AND ANALYSIS TECHNIQUES

To measure the poloidal variation of the high-Z impurity density, the (R, Z) structure of the photon emission was measured using multiple horizontally viewing pinhole cameras, each employing an unfiltered AXUV-22EL photodiode array.[43] The details of the instrumentation and the calibrations are described in Ref. 44 and Appendix B of Ref. 16,

with Figure 2 displaying their tangency radii, R_T, with respect to a typical H-mode equilibrium. Each array measures the brightness profile at a different height, $B(R_T, Z_o)$ and by assuming toroidal symmetry can be inverted to find the local volumetric emission, $\varepsilon(R, Z_o)$. Tangency radii for two mid-plane arrays, AXA (closed circles) and AXJ (open circles) are offset for clarity in Figure 2, but both measure at $Z_o \simeq 1$ cm at two separate toroidal locations. Using the magnetic equilibrium, the emissivity on the LFS can be compared to that of the HFS on the same flux-surface, allowing each pinhole camera to independently measure the in/out asymmetry. By combining data from multiple cameras, discussed below, up/down asymmetries can be found as well as higher order poloidal variation. This diagnostic layout is ideally suited for examining asymmetry structure in the core, $r/a < 0.8$, of tokamak plasmas, in contrast to most tomography diagnostics which are arranged in a poloidal plane.[45–47] In those systems, emission from the divertor region, or
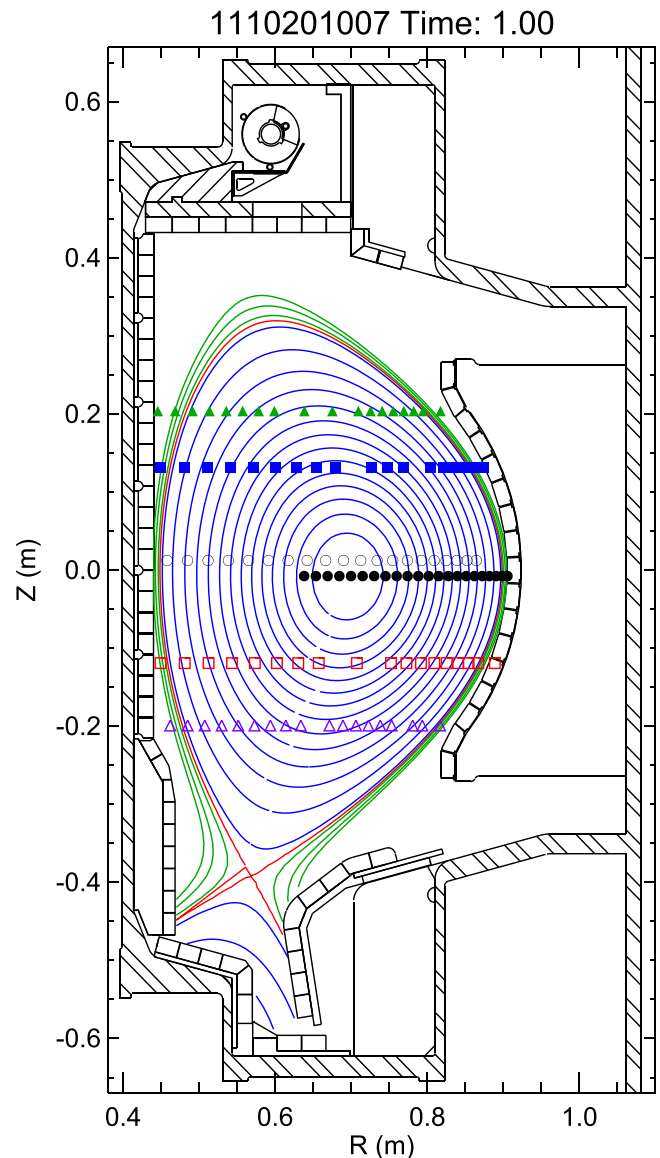

FIG. 2. The tangency radii of the pinhole cameras plotted over an H-mode equilibrium reconstruction; AXA ($\bullet$), AXJ ($\circ$), WB1AX ($\blacktriangle$), WB2AX ($\blacksquare$), WB3AX ($\square$), and WB4AX ($\triangle$).

localized, poloidally varying low-Z emission near the boundary will pollute the signal coming from high-Z asymmetries. Additionally, the geometry of the tokamak generally favors views from the LFS toward the HFS which, when arranged poloidally rather than horizontally, work to reduce sensitivity to in/out emission asymmetries.

Example observations from the midplane arrays, AXA and AXJ, are shown in Figure 3, plotting emissivity versus major radius on the left, and using EFIT[48] to plot AXJ emission versus normalized minor radius, r/a, for the LFS (purple) and the HFS (orange). The AXA and AXJ pinhole cameras are independently operated and calibrated and, assuming toroidal symmetry, observe the same plasma profile. The good agreement between these two sets of data demonstrates the accuracy required to combine the off-midplane pinhole cameras into a single set of data to compute quantitative up/down

asymmetries. Figure 3(a) plots the emissivity profiles for molybdenum injected via laser blow-off[49] into an Ohmic L-mode, demonstrating little to no in/out asymmetry, as expected. In Fig. 3(b), the same plot is shown for the steady-state emissivity in an ICRF-heated EDA H-mode. Here, core intrinsic rotation is relatively strong, $v_{\phi,0} \sim 70 \, \text{km/s}$, and ICRF power density, P_{RF}/n_e, is weak due to the high density, resulting in substantial accumulation on the LFS of a flux surface, consistent with inertia. In Fig. 3(c), the emissivity is plotted for a low-density, ICRF-heated L-mode plasma where intrinsic flow is weak, $v_{\phi,0} < 10 \, \text{km/s}$, but low field side, off-axis D(H) heating drives a strong minority anisotropy, consistent with observed HFS peaking of emissivity.

To quantitatively determine the poloidal variation, the equilibrium reconstruction is used to map the profiles to minor radius, determining $\varepsilon(r/a)$. EFIT provides the (R, Z) points of each flux surface for 33 r/a locations evenly spaced in normalized poloidal flux, ψ_n. At each EFIT radial location, the inverted profile is interpolated to find (θ_o, ε) points from each array. The emissivity on each flux surface is expanded in a low order Fourier series

$$\varepsilon(\theta) = a_0 + a_1 \cos\theta + a_2 \sin\theta + a_3 \cos 2\theta + a_4 \sin 2\theta, \tag{12}$$

where θ is defined in the geometrical sense relative to the magnetic axis. The coefficients a_0-a_4 are determined by a linear-least squares fit of Eq. (12) to experimental (θ_o, ε) data. In regions of the plasma where only AXA and AXJ are available, only a_0 and a_1 are used. When both WB2 ($Z = +12.5$ cm) and WB3 ($Z = -12.5$ cm) are available, a_0-a_2 are used, with the inclusion of the $m = 2$ terms being optional in regions where data from WB1 ($Z = +20.4$ cm) and WB4 ($Z = -20.4$ cm) are available.

This analysis technique is applied to the EDA H-mode shot shown in Figure 3(b). The AXA, AXJ, WB2AX, WB3AX, and WB4AX are all used to find the radial profiles of a_0, a_1, and a_2, and in Figures 4(a) and 4(b), $\varepsilon(\theta)/\varepsilon(0)$ are shown at r/a of 0.6 and 0.8, respectively. The off-midplane arrays are consistent with those on the midplane at midradius, but closer to the edge, at $r/a = 0.8$, higher order variation in the poloidal structure is starting to become evident. In Figure 4(c), the computed in/out asymmetry is compared with results using Eq. (10) from Ref. 10 which uses only the midplane arrays. For $r/a < 0.45$, only AXA and AXJ data are constraining the fit and the good agreement is not surprising. Between $0.45 < r/a < 0.7$, WB2AX and WB3AX are also included, and both techniques find the same asymmetry within error bars. For $r/a > 0.7$, WB4AX is added, and the two techniques begin to quantitatively disagree, although both show a drop and possibly even a reversal of the sign in the in/out asymmetry as $r/a \to 1$. Using this technique has been shown to be insensitive to the shape of the flux-surface averaged emissivity profile,[16] allowing both peaked and hollow a_0 profiles to carry information on the in/out ($n_{z,cos}/\langle n_z \rangle = a_1/a_0$) and up/down ($n_{z,sin}/\langle n_z \rangle = a_2/a_0$) asymmetries profiles.

These measurements are of the poloidal variation in the total emissivity of the plasma, $\varepsilon_{total} = \sum_j n_e n_j L_j(T_e)$, where
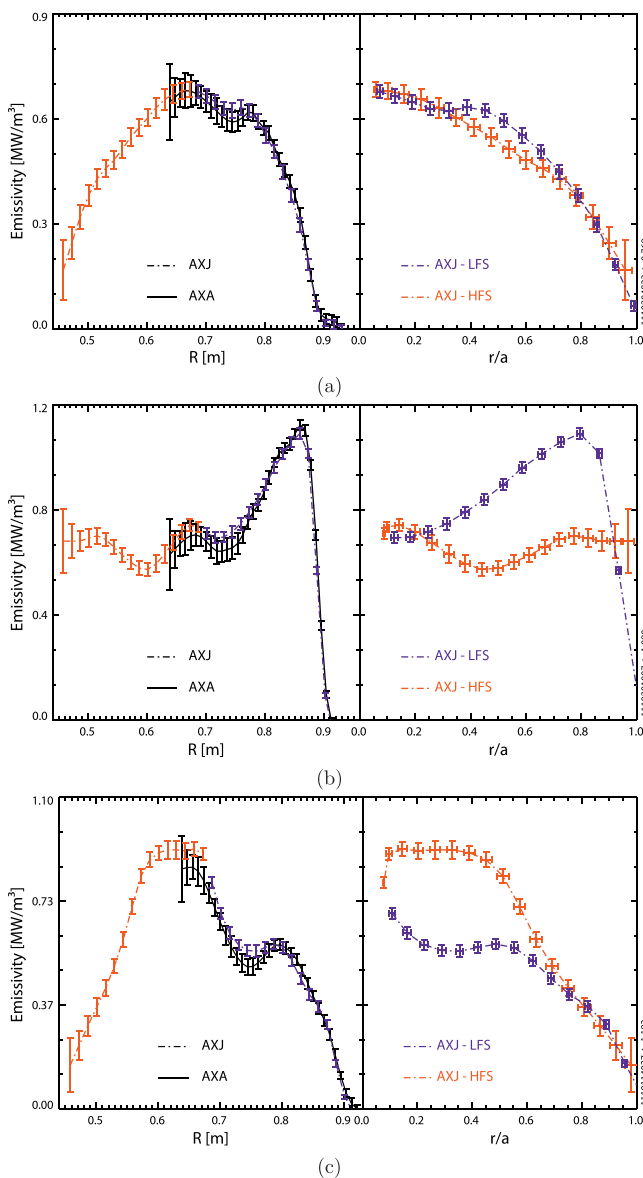

FIG. 3. Measured midplane emissivity profiles show qualitative agreement with expected asymmetries. During a Mo LBO injection into an Ohmic plasma (a), little to no asymmetry is observed. An ICRF-heated EDA H-mode (b) displays strong LFS accumulation, while a low-density ICRF-heated L-mode plasma (c) reveals enhanced HFS emission.
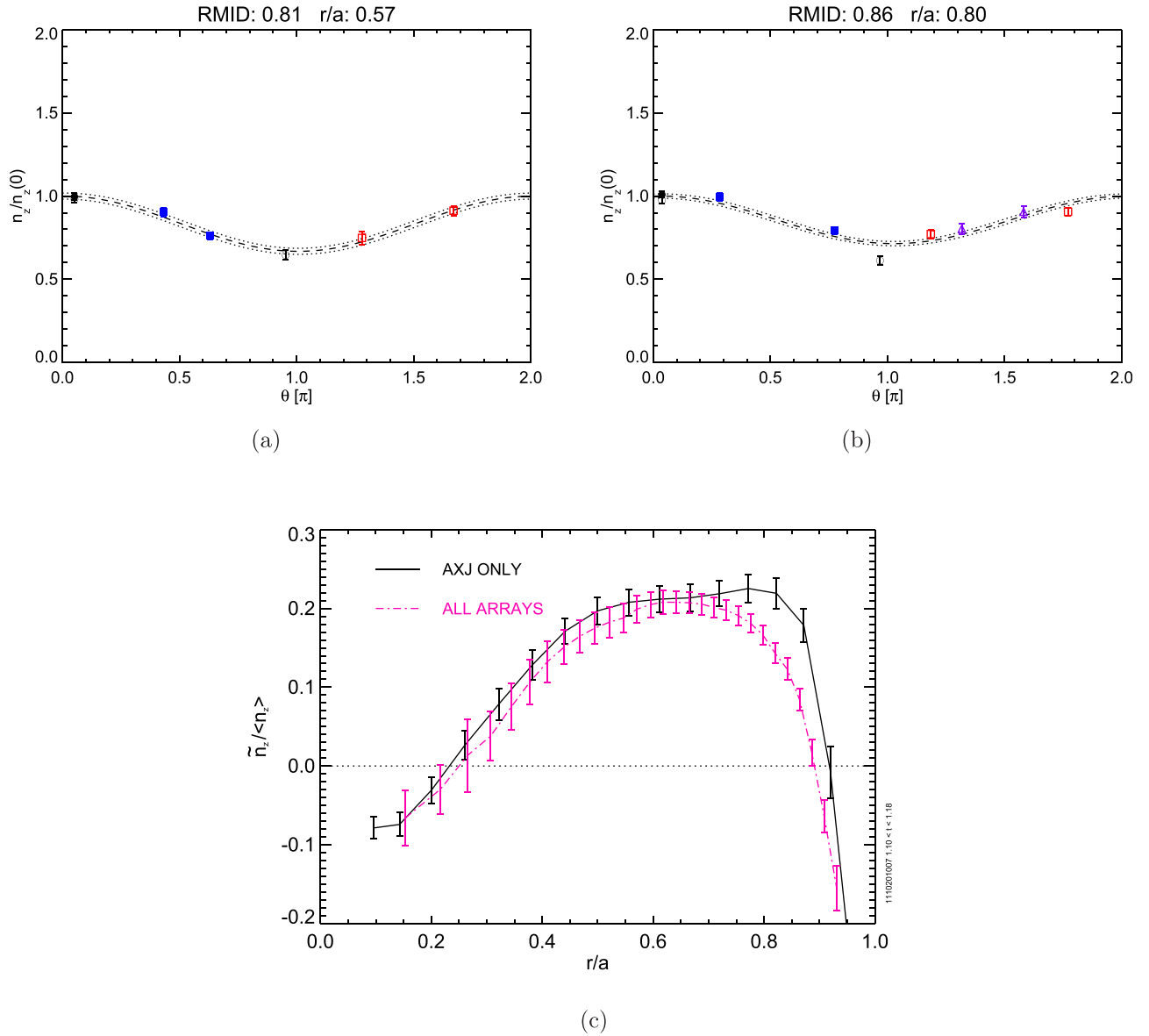
FIG. 4. Plots of measured emissivities and fits of poloidal variation at various $r/a = 0.6$ (a) and 0.8 (b) for the profile shown in Figure 3(b); AXA (●), AXJ (○), WB2AX (■), WB3AX (□), and WB4AX (△) with a comparison between methods (c).

n_j is an ion species and L_j is the electron temperature dependent radiative efficiency. In order to convert measurements of $\tilde{\varepsilon}_{total}/\langle\varepsilon_{total}\rangle$ to $\tilde{n}_z/\langle n_z\rangle$, assumptions about what's driving the radiation variation must be made. Using VUV/SXR spectroscopy, discharges and time slices are selected where a single high-Z species is contributing the bulk of the emission, $\varepsilon_{total} = \delta\varepsilon + \varepsilon_z$. The measured asymmetry of the total emission can then be interpreted as that of the high-Z impurity, taking into account the fraction of emission that is due to lower-Z emission, assumed to have smaller or negligible poloidal variation

$$\frac{\tilde{\varepsilon}_{total}}{\langle\varepsilon_{total}\rangle} = \frac{\langle\varepsilon_z\rangle}{\langle\delta\varepsilon + \varepsilon_z\rangle}\frac{\tilde{\varepsilon}_z}{\langle\varepsilon_z\rangle}. \tag{13}$$

All discharges discussed in this research have been selected for strong molybdenum emission where $\varepsilon_{Mo}/\varepsilon_{total} \geq 90\%$, but no attempt at correcting for this systematic error using Eq. (13) has been made since the uncertainty in the

measured asymmetry due to the Abel inversion generally dominates.

Parallel heat transport will ensure that T_e is constant on a flux surface and by normalizing to the flux-surface averaged emissivity, $\langle\varepsilon_z\rangle$, $L_z(T_e)$ cancels. Similarly, electron density is expected to be a flux function for low main-ion Mach number plasmas, $M_i^2 < 0.1$, with small poloidal electric fields, $e\tilde{\Phi}/T_e \ll 1$, such as the ICRF-heated, intrinsically rotating C-Mod plasmas. This lack of poloidal variation in n_e has been confirmed by comparing Thomson scattering density measurements along a vertical chord at $R = R_o$ and interferometry data for vertical chords for $R > R_o$. This allows $\tilde{\varepsilon}_{total}/\langle\varepsilon_{total}\rangle$ to be equivalent to $\tilde{n}_{Mo}/\langle n_{Mo}\rangle$ in a wide range of C-Mod plasmas.

IV. MEASURED AND PREDICTED C-MOD IMPURITY ASYMMETRIES

In ICRF-heated C-Mod plasmas, the large in/out asymmetries that have been observed, such as those shown in Figure 3,

have been shown to be driven, primarily, by the centrifugal force and the poloidal variation of the electrostatic potential.[10] While that study included only data from the midplane diode arrays, the research has since been extended to include the off-midplane arrays for the same discharges.[16] No significant change in the $n_{z,cos}/\langle n_z \rangle$ profile was found and no change in the $n_{z,sin}/\langle n_z \rangle$ profile was observed when the rf heating was removed, confirming that the ICRH drives only an in/out asymmetry and not an up/down asymmetry. Additionally, the smooth poloidal variation in $n_z(\theta)/n_z(\theta = 0)$ predicted by the theory developed in Ref. 10 is reproduced by the experiment as shown in Figure 5. Within the resolution of the 2D reconstruction, there is no evidence of off-midplane peaking of the asymmetry and the poloidal variation is well-described by low-order Fourier components, consistent with LFS-heating simulations in Ref. 50.

In both Ohmic and auxiliary-heated plasmas, a small, $\tilde{n}_z/\langle n_z \rangle \leq 0.1$, up/down asymmetry is regularly observed. As discussed in Sec. II, comprehensive parallel impurity transport theory for the banana regime[7] predicts that the up/down asymmetry is driven by ion/impurity friction but also depends on the toroidal rotation. This can be thought of as qualitatively as friction smearing an in/out asymmetry driven by centrifugal force, causing a minor accumulation in the direction of the parallel flow.

Both up/down and in/out asymmetry profiles have been computed numerically including ion-impurity friction, ICRH effects and the centrifugal force for EDA H-mode plasmas,[51] and a kinetically constrained EFIT reconstruction is used. In these cases, the well motivated assumption of $T_e = T_i$ is used to reduce the uncertainty in the temperature profile going into the friction calculation since the difference between the density and temperature scale lengths is required. Figure 6(a) shows that between $0.5 < r/a < 0.8$, there is substantial disagreement between the predicted up/down asymmetry and the measurement. Because of the flat density and peaked temperature profile, $n_{z,sin}/\langle n_z \rangle < 0$ is predicted over the core plasma, while $n_{z,sin}/\langle n_z \rangle > 0$ is observed. Good agreement is found between measurements and predictions displayed in Figure 6(b), where the in/out asymmetry is due primarily to

FIG. 6. Profiles of experimental up/down and in/out asymmetry in the 0.9 MA EDA H-mode, compared to modeling including inertia, friction and ICRH effects.

centrifugal effects and the inclusion of the friction does not substantially change the modeling results.

Two analytical theories predict the up/down asymmetry in the circular, low inverse-aspect ratio limit. Fülöp and Helander,[7] represented by Eq. (11) and the work in Brau *et al.*[3] modeled by $n_z(\theta, r) = n_{z,o}(r)(1 + \eta_{qf} \sin \theta)$, with η_{qf} given by Eq. (2) in that reference. As a consistency check, C-Mod measurements are compared to both of these simplified forms rather than the 1D parallel transport code. The data set is restricted to EDA H-modes where the $T_e = T_i$ assumption is most accurate and spline fits to T_e measured using Thomson and ECE are used. A comparison of measurements to n_s and η_{qf} for $\Delta r/a \simeq 0.05$ from $0.55 < r/a < 0.85$ is shown in Figure 7. Both trends overlap and predict substantial impurity accumulation in the direction of the ion ∇B drift direction. As the modeled asymmetry increases in magnitude, measurements show the plasma becoming more up/down symmetric, yet small, $n_{z,sin}/\langle n_z \rangle < 0.1$ accumulation opposite to the ion ∇B drift direction is observed in plasmas where n_s and η_{qf} are predicted to be near zero.

This parallel impurity transport modeling indicates that strong accumulation of impurities in the direction of the ion ∇B drift should be seen in C-Mod plasmas. This is counter to the heuristic picture of the up/down asymmetry being
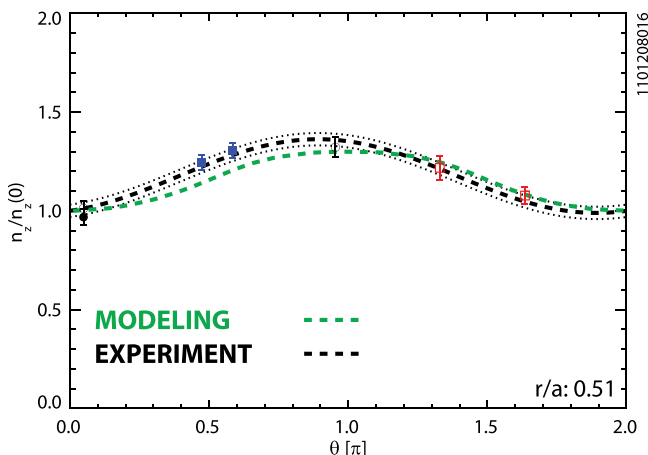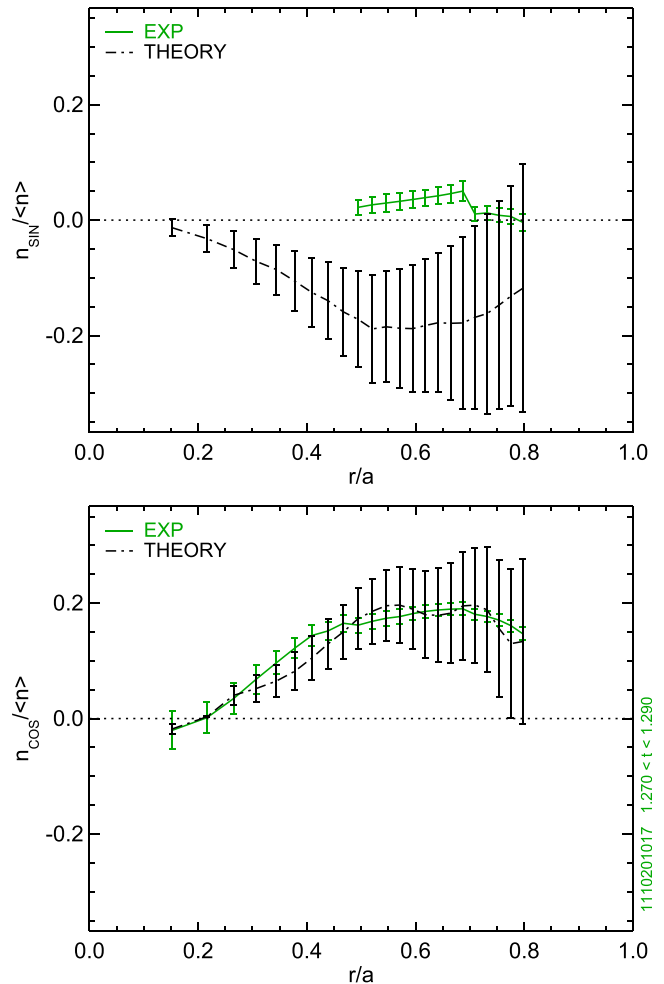

FIG. 5. Comparison of $n_z(\theta)/n_z(0)$ measurements (black-dashed) to theory in Ref. 10 (green-dashed) for plasma with LFS heating near the resonance layer; AXA (●), AXJ (○), WB2AX (■), WB3AX (□).
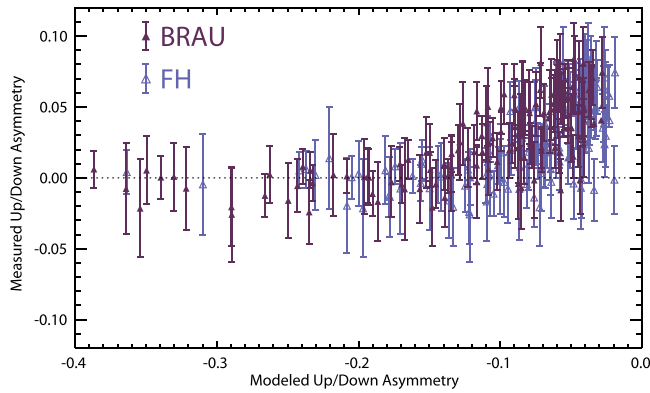
FIG. 7. Comparison of two circular, low inverse-aspect ratio analytical models for the up/down asymmetry in EDA H-modes for $0.55 < r/a < 0.85$. Neither matches experimental results.

driven by impurity entrainment in the Pfirsch-Schlüter return flow. Theory predicts this can only occur in the banana regime, only when the ion temperature gradients are stronger than twice the density gradient, $L_{T_i}^{-1} > 2L_{n_i}^{-1}$.[7] That this occurs in C-Mod H-mode plasmas is consistent with historical observations for standard EDA H-modes, where the electron density profiles are flat inside the pedestal,[52] but temperature profiles are peaked on axis. In most cases, the observed asymmetries are in the opposite sense, $n_{z,sin}/\langle n_z \rangle > 0$, with trends indicating the largest positive values seen when the up/down asymmetry is predicted to be weaker. This indicates that another physical process may be at work to accumulate impurities away from the ion ∇B drift direction when ion-impurity friction is weak. This mechanism must also be large enough to balance or circumvent the ion-impurity friction in cases where predicted impurity asymmetries are large, $n_s \sim -0.3$, while observations show them to be relatively small, $|n_{z,sin}/\langle n_z \rangle| \leq 0.05$.

In Figure 8, the measured up/down asymmetry for a collection of Ohmic, I-mode and H-mode plasmas is plotted against the $\nu_* = \nu_{ii}/\omega_{tr,i}/\epsilon^{3/2}$, where $\nu_* > 1$ indicates a transition from the banana to the plateau regime. As the collisionality increases and approaches $\nu_* \simeq 1$, the weak impurity accumulation opposite the ion ∇B drift direction

decreases and impurity density is measured to be more up/down symmetric. The larger asymmetries are well into the banana regime, confirming that comparisons between measurements and modeling have been completed for the correct collisionality.

V. LINK BETWEEN IMPURITY ASYMMETRIES AND POLOIDAL ROTATION

The friction is dependent on the relative velocity between the ions and impurities, and in order to investigate the discrepancy between the measured and modeled up/down asymmetries, it is worth looking closer into the neoclassical predictions for ion and impurity poloidal rotation. In the first order velocity equation for an ion species (3), the field aligned flow term, $K_a(\psi)/n_a\mathbf{B}$, is found by solving the parallel force balance equation. For the impurities, this is accomplished by solving the same parallel transport equation being used to find the impurity density variation. The $v_{\theta,z}$ profiles that are output from the code described in Appendix are therefore self-consistent with the predicted poloidal asymmetry. This means that in the poloidal flow of the impurities, not only is there an explicit dependence on the poloidal variation due to the density, $n_z(\psi, \theta)$ but also an implicit dependence from K_z which is sensitive to the magnitude of the impurity asymmetries as shown in Ref. 7. While there is also an explicit dependence on n_a in the solid body toroidal rotation in Eq. (3) as well, the $1/Z_a$ scaling of the diamagnetic flow results in an ignorable contribution for high-Z impurities relative to the $\mathbf{E} \times \mathbf{B}$ flow.

For main-ions in the banana regime, the poloidal flow, $v_{\theta,i} = u_i B_\theta$, is found by solving the drift-kinetic equation[7] or using a moment approach[53] to obtain (9) within a constant. In impure plasmas, $Z_{eff} \geq 2$, the ion-impurity friction can start to play an important role in determining $v_{\theta,i}$, generally requiring a numerical approach to solve the coupled multi-species transport equations. Existing tools have simplifying assumptions, such as in the NCLASS code,[54] commonly used to calculate neoclassical poloidal flows, where the impurity density is forced to be a flux function. The NEO[55] and GTC-NEO[56] codes solve the drift-kinetic equation for ions and impurities up to second order in ρ_i/a, but ion-impurity collisional effects are not included in the lowest order impurity momentum balance. This ordering for the impurities is similar to the weak ordering discussed in Ref. 25, making it unclear if such codes reproduce asymmetries driven by friction. While NEO accounts for poloidal redistribution due to the centrifugal force, no poloidal electric fields due to cyclotron or beam heating are included. Recent experiments on DIII-D[57] have also demonstrated disagreements between neoclassical predictions and measurements of main-ion poloidal flow.

A verification effort of these codes to analytical theory in the circular low-aspect ratio limit[7] is suggested as future work, with the focus of this research being the sensitivity of asymmetry physics to the magnitude of the main-ion poloidal flow. This is accomplished by artificially changing the magnitude of the $g\gamma$ term in the numerical solution of the trace limit 1D impurity transport code discussed in the Appendix. Although a weak constraint on the impurity poloidal rotation
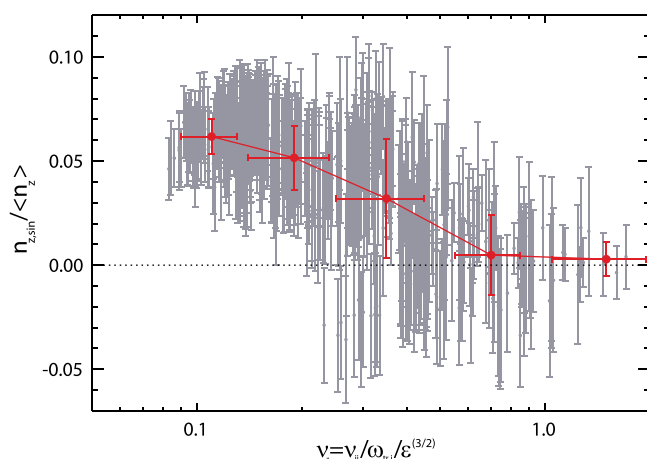

FIG. 8. Correlation of the measured up/down asymmetry with collisionality, ν_*, with the full data set (gray) and binned and averaged data (red).
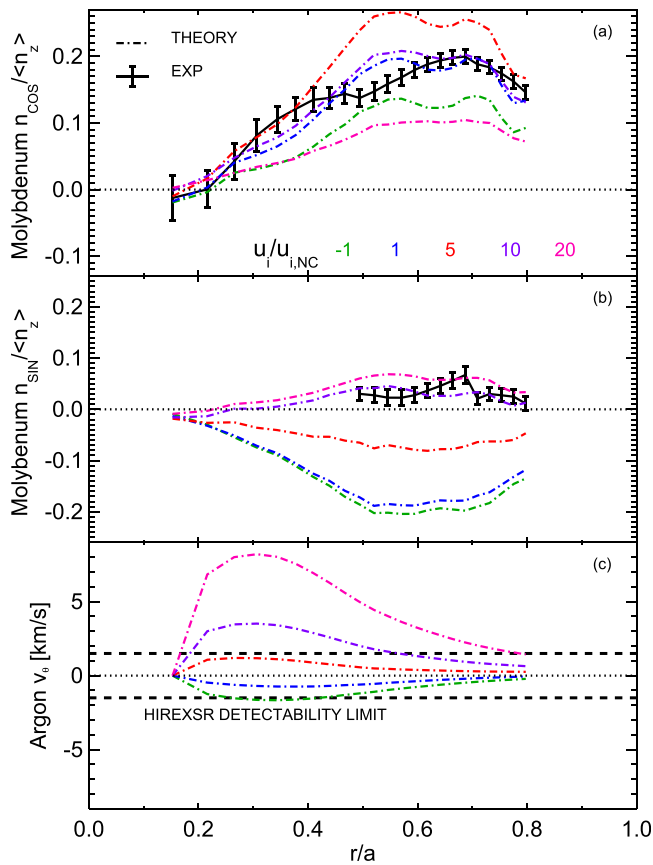
FIG. 9. Change in the molybdenum asymmetry profiles and the argon poloidal rotation for various assumptions of the main ion poloidal flow.

is provided by XICS,[42] no measurement of the main ion flow is available. Figure 9 shows the effect changes in u_i have on the in/out and up/down asymmetries as well as the poloidal rotation. This is completed for the EDA H-mode shown in Figure 6 where the asymmetry is due to molybdenum, but the poloidal rotation is estimated from Ar^{16+} emission. For each $u_i/u_{i,NC}$, the parallel transport code is run for molybdenum to find the $n_{z,cos}/\langle n_z \rangle$ (a) and $n_{z,sin}/\langle n_z \rangle$ (b) profiles, and run again for argon to find $v_{\theta,z}$ (c), plotted for the outboard midplane. The up/down asymmetry is shown to change monotonically with u_i/u_{NC} in this range, while the in/out asymmetry increases and then decreases. This is due, numerically, to the non-linear dependence of $n_{z,cos}/\langle n_z \rangle$ on γ (10) and the fact that γ is negative. Physically, this could be interpreted as poloidal flow becoming so strong that is smears out any asymmetries driven by the centrifugal force.

It is clear from these results that both the up/down asymmetry and the impurity poloidal flow are sensitive to the main ion poloidal rotation. The best agreement is found for $u_i/u_{i,NC} = 10$, where the modeled in/out and up/down asymmetries are both in reasonable agreement with measurement. But, forcing $u_i/u_{i,NC} = 10$ results in $v_{\theta,z}$ for argon of 3-4 km/s at $r/a \simeq 0.3$, while XICS measurements are in 1-2 km/s range for $r/a < 0.5$, in disagreement with predictions.

Previous experimental tests of poloidal impurity rotation[58–60] show that agreement between theory and experiment has not yet been consistently demonstrated in the core of collisionless tokamak plasmas. The link

established between $v_{\theta,z}$ and $n_z(\theta)$ suggests a much more stringent test would be to simultaneously demonstrate that both measured flows and up/down asymmetries agree with predictions. The most widely used method to find $v_{\theta,z}$ is charge-exchange recombination spectroscopy using midplane neutral beams, a technique that may not be able to meet this challenge. While this technique is being extended to measure the HFS midplane velocities and densities,[61,62] the up/down asymmetry is most sensitive to the ion-impurity friction. Future work at C-Mod will focus on using XICS to measure both up/down asymmetries and flows in molybdenum in combination with the tools described here to measure in/out asymmetries.

VI. SUMMARY

This paper describes empirical and computational efforts to validate neoclassical parallel transport theory for high-Z impurities in tokamak plasmas. While observations of strong in/out asymmetries in molybdenum density can be accurately described by inertia and poloidal electric fields, measurements of up/down asymmetries disagree with predictions based on ion-impurity friction. Up/down asymmetries $-0.05 < n_{z,sin}/\langle n_z \rangle < 0.10$, are observed over $0.5 < r/a < 0.9$, with $n_{z,sin} > 0$ corresponding to accumulation opposite the ion ∇B drift direction, while predictions of $-0.4 < n_{z,sin} < 0$ are estimated for EDA H-mode plasmas using multiple transport models. Artificially modifying main-ion flow in parallel transport simulations is shown to affect both $n_z(\theta)$ and $v_{\theta,z}$, and simultaneous agreement between measured and predicted up/down and in/out asymmetry as well as impurity poloidal rotation is not obtained. This link between poloidal flow and poloidal impurity density variation describes a more stringent test for parallel neoclassical transport theory for future validation experiments.

APPENDIX: NUMERICAL CODE TO COMPUTE $n_z(\theta)$

The method is based on the work of Fülöp and Helander for a trace, $n_z Z^2/n_i \leq 1$, high-Z impurity in the collisional[8] and collisionless[7] main ion regimes with the following additions. First, the published work in the collisional regime does not include the effect of centrifugal force. As the form of the differential equation is the same for both regimes, it is straightforward to add. For the high-Z impurity, the toroidal rotation is assumed to be due to $E \times B$ flow, and including it does not change $v_{z,\parallel} - v_{i,\parallel}$ which drives the ion-impurity friction. Second, the effects of a minority species with an anisotropic pressure tensor are included as detailed in Ref. 10.

The EFIT code is used to reconstruct the magnetic equilibrium by solving the Grad-Shafranov equation to determine $\psi(R,Z)$. The axisymmetric magnetic field is represented by

$$\vec{B} = I(\psi)\nabla\phi + \nabla\psi \times \nabla\phi, \qquad (A1)$$

where $\nabla\phi = R\hat{\phi}$ and $I(\psi)$ are determined by EFIT. The standard C-Mod EFIT reconstruction solves for 33 points evenly spaced in poloidal flux between the magnetic axis and the last closed flux surface or $0 \le \psi_n \le 1$. At each ψ_n value, the (R,Z) points which describe the shape of the flux surface are provided. The poloidal angle, θ, is defined relative to the magnetic axis as shown in Figure 10(a).

$$r = \sqrt{(R - R_{ax})^2 + (Z - Z_{ax})^2}, \qquad (A2)$$

$$\theta = \arctan\left(\frac{Z - Z_{ax}}{R - R_{ax}}\right) \qquad (A3)$$

with R_{ax} and Z_{ax} the location of the magnetic axis. The poloidal field, B_p, and the toroidal field, B_t, are known at each location along the flux surface. Note that even though the poloidal angle is defined in the naive, geometrical sense, the circular approximation is not being used and the flux surface shaping is kept in the $\vec{B} \cdot \nabla\theta$ term. This differs from the notation of Refs. 7 and 8. From Figures 10(b) and 10(c), $\vec{B} \cdot \nabla\theta$ can be derived to be
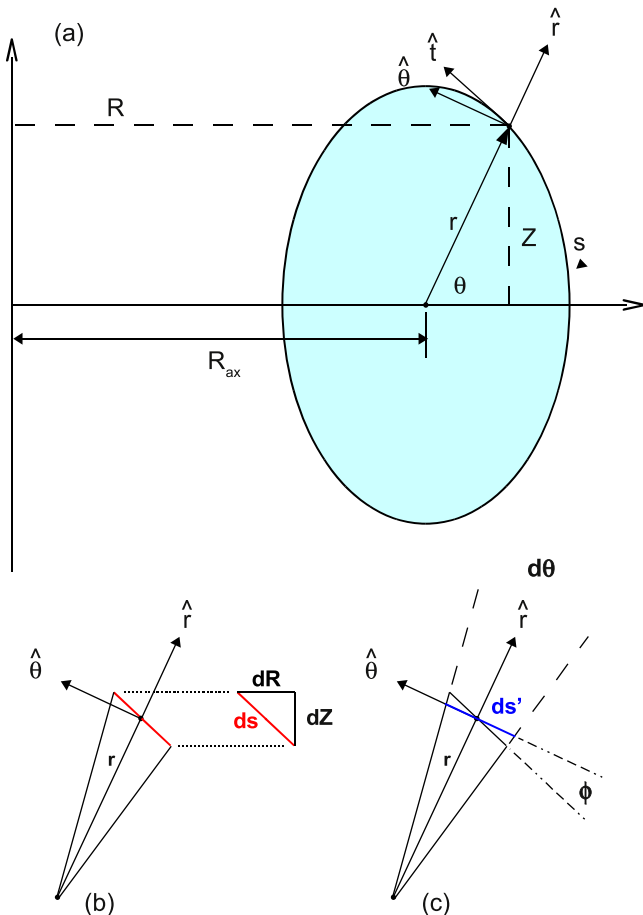

(a)

FIG. 10. Geometry used in calculating the solution to the 1D parallel impurity transport equation.

$$\vec{B} \cdot \nabla\theta = \frac{B_p \cos\phi}{r}, \qquad (A4)$$

$$\vec{B} \cdot \nabla\theta = B_p \frac{\sin\theta - m(\theta)\cos\theta}{r\sqrt{m(\theta)^2 + 1}} \qquad (A5)$$

with $m(\theta) = dZ/dR$, the instantaneous slope along the flux surface. For a circular plasma, this reduces to B_p/r as expected. As described in Sec. II, the 1D inhomogeneous nonlinear differential equation for the parallel force balance on a flux surface is of the form

$$(1 + \alpha_z n)\frac{\partial n}{\partial\theta} = X(\theta)n + K_z Y(\theta), \qquad (A6)$$

where $n = n_z/\langle n_z \rangle$, $\alpha_z = Z^2\langle f_z \rangle/(T_i/T_e + n_i/n_e)$, and K_z is determined using the periodic boundary condition, $n(0) = n(2\pi)$. This can be reduced to a simpler linear differential equation with the restriction that $\alpha_z \ll 1$

$$\frac{\partial n}{\partial\theta} = X(\theta)n + K_z Y(\theta). \qquad (A7)$$

The largest impact of a finite impurity density is to reduce the magnitude of the asymmetry by including it in quasi-neutrality. This effect is kept in via Z_{eff} terms in $X(\theta)$, which also account for other background impurities. This limit ignores the impact on the ion-impurity friction that arises due to impurities modifying the main-ion flow as well as the possibility of impurity-impurity friction.

The solution to Eq. (A7) can be determined using an integrating factor, $\exp(\mu) = \exp(\int_0^\theta X(\theta)\,d\theta)$ reducing Eq. (A7) to

$$s\frac{\partial}{\partial\theta}[\exp(\mu(\theta))n(\theta)] = -K_z Y(\theta)\exp(\mu(\theta)). \qquad (A8)$$

Integrating and applying the periodic boundary condition allows $n(\theta)$ to be expressed as

$$\frac{n(\theta)}{n(0)} = \exp(-\mu(\theta))\left(1 - \frac{1-\alpha}{\beta}\int_0^\theta Y(\theta)\exp(\mu(\theta))\,d\theta\right), \qquad (A9)$$

where $\alpha = \exp(-\mu(2\pi))$ and $\beta = \int_0^{2\pi} Y(\theta)\exp(\mu(\theta))\,d\theta$. The poloidally varying X function is determined separately for each main-ion collisionality regime, $\hat{\nu}_{ii} = \nu_{ii}/\omega_{tr,i}$, where the ion-ion collisionality is $\nu_{ii} = 3\sqrt{\pi}/4\tau_{ii}$ and the ion transit frequency is $\omega_{tr,i} = v_{th,i}/qR_o$. The low-collisionality or banana-regime is $\hat{\nu}_{ii} \ll 1$, and the high-collisionality or Pfirsch-Schlüter regime is $\hat{\nu}_{ii} \gg 1$. The $Y(\theta)$ term is the same for both

$$Y(\theta) = \frac{m_i Z^2}{\tau_{ii} T_i} \frac{B^2}{\vec{B} \cdot \nabla\theta}, \qquad (A10)$$

where $B^2 = B_p^2 + B_t^2$ and $\vec{B} \cdot \nabla\theta$ is from Eq. (A5). For both collisionalities, $X(\theta)$ is broken into 4 parts, X_1, X_2, X_3, and X_4, where X_3 and X_4 are independent of $\hat{\nu}_{ii}$

$$X_3 = -\frac{m_z \omega_z^2}{2T_i}\left[1 - Z\frac{\omega_i^2}{\omega_z^2}\frac{m_i}{m_z}\frac{Z_{eff}T_e}{Z_{eff}T_e + T_i}\right]\frac{\partial R^2}{\partial \theta}, \quad (A11)$$

$$X_4 = Zf_m\frac{T_e}{Z_{eff}T_e + T_i}\left\langle\frac{1}{B^\eta}\right\rangle^{-1}\frac{(-\eta)}{B^{-(\eta+1)}}\frac{\partial B}{\partial \theta} \quad (A12)$$

with f_m being the minority ion fraction, n_m/n_e, $\eta = (T_\perp/T_\parallel - 1)$ is the minority's temperature anisotropy and $\langle...\rangle$ is the standard flux surface average. The main ion toroidal rotation, ω_i, will always be slightly larger in the co-current direction relative to the impurity rotation due to diamagnetic flow but to quantitatively include this in the theory is beyond the scope of this work. In all cases, $\omega_i = \omega_z$ is assumed. For main ions in the banana regime,

$$X_1 = \frac{m_i I Z^2}{\tau_{ii}e}\left(\frac{n_i'}{n_i} - \frac{1}{2}\frac{T_i'}{T_i}\right)\frac{1}{\vec{B}\cdot\nabla\theta}, \quad (A13)$$

$$X_2 = \frac{f_c m_i I Z^2}{3\tau_{ii}e\langle B^2\rangle}\frac{T_i'}{T_i}\frac{B^2}{\vec{B}\cdot\nabla\theta}, \quad (A14)$$

where $f_c = 1 - 1.46\sqrt{\langle r\rangle/R_o}$ is the circulating fraction taken from Ref. 17 and prime denotes derivative with respect to ψ. The X_1 term is related to the g term and X_2 is related to the product of γ and g from Refs. 7 and 8. For simplicity, the trace-limit expression for γ is used in X_2 which avoids the need for velocity-space integrals in the main ion solution which would be needed to correct the ion-impurity friction for $\alpha_z \sim 1$. For main ions in the Pfirsch-Schlüter regime,

$$X_1 = \frac{m_i I Z^2}{\tau_{ii}e}\frac{n_i'}{n_i}\frac{1}{\vec{B}\cdot\nabla\theta}, \quad (A15)$$

$$X_2 = \frac{2.8m_i I Z^2}{\tau_{ii}e\langle B^2\rangle}\frac{T_i'}{T_i}\frac{B^2}{\vec{B}\cdot\nabla\theta}. \quad (A16)$$

The primary difference in the collisionalities is the weighting of the gradient scale length terms. For low $\hat{\nu}_{ii}$ plasmas, the ion-impurity friction is proportional to the difference between the density and temperature scale lengths. In practice, for $r/a < 0.9$, the kinetic profile scale lengths are of similar magnitude with L_n is less than L_T, so the X_1 from Eq. (A13) is usually near zero. In contrast, these two terms add together for high collisionality plasmas making them more likely to impact parallel force balance as $\hat{\nu}_{ii}$ is increased.

Solutions to Eq. (A7) can be compared to analytic predictions in order to verify the code. For weak ion-impurity friction, $\alpha_z = 0$, and no minority effects, there exists an exact solution for the poloidal density variation with respect to major radius, R, for a trace impurity in a rotating plasma[4,5]

$$\frac{n(\theta)}{n(0)} = \exp\left[\frac{m_z\omega^2(R(\theta)^2 - R(0)^2)}{2T_z}\left(1 - Z\frac{m_i}{m_z}\frac{T_e}{T_e + T_z}\right)\right]. \quad (A17)$$

In Ref. 10, analytical solutions were derived for $n_z/\langle n_z\rangle$ sustained by a poloidal electric field due an anisotropic minority species, and the combination of the centrifugal force and an anisotropic species. For cases with combined inertial and ion-impurity friction forces,[7] the authors have expanded n in a Fourier series, in the $\epsilon \ll 1$ circular cross-section limit to find the leading order $m = 1$ terms with $n = 1 + n_c\cos\theta + n_s\sin\theta$,[7] given by Eqs. (10) and (11) in Sec. II. Uncertainty is determined analytically from Eqs. (10) and (11) via standard error propagation assuming uncorrelated error in the input kinetic profiles, n_i, T_e, T_i, and ω. This fractional error is then assumed to be the same for the in/out and up/down asymmetries derived from solving (A7) numerically. In the limit of $g \gg 1$, or very large gradients, an approximate solution to order g^{-2} is found to be[6,8]
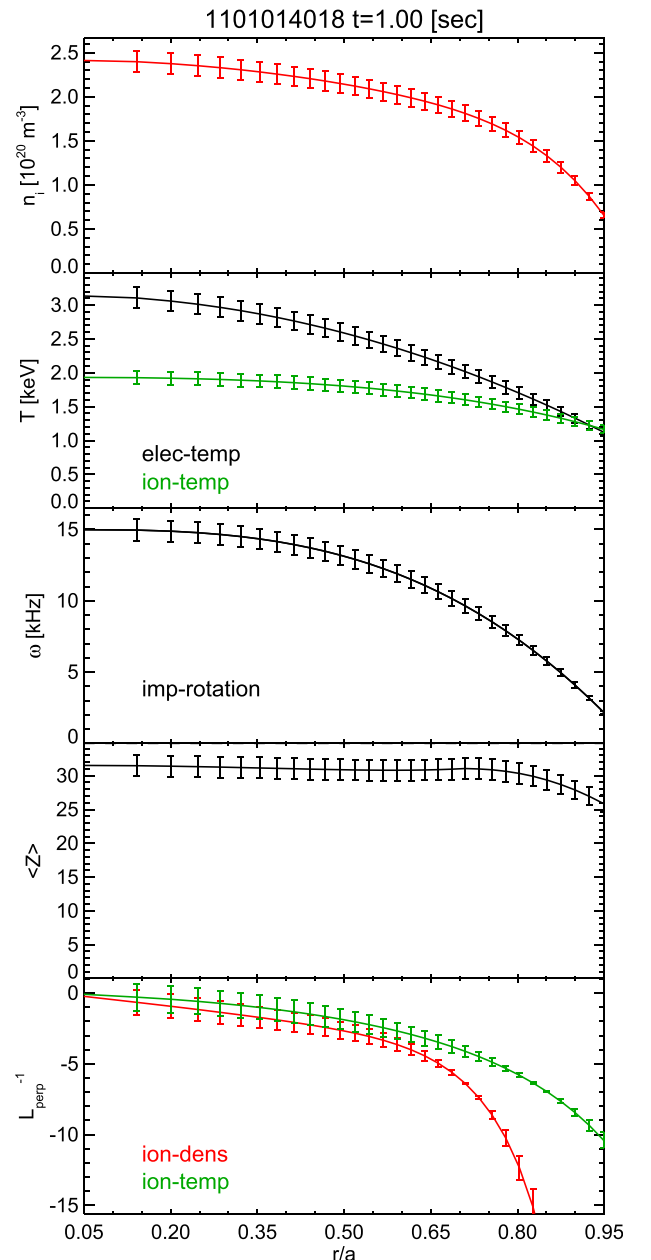

FIG. 11. Input profiles used for comparing 1D asymmetry code to theoretical limits.

$$n_0 = \frac{\gamma}{1 - \langle(1 + \gamma b^2)^{-2}\rangle} \frac{b^2}{1 + \gamma b^2}, \qquad (A18)$$

where $b^2 = B^2/\langle B^2\rangle$. In this limit, impurity density is accumulated where the magnetic field is strongest, at the inboard side.

To verify the code against these analytical solutions, we use experimental EFIT reconstructions with arbitrary kinetic profiles, selected to highlight different physics. Two equilibria are used; a near-circular, Ohmic, low-β plasma ($\beta_p = 0.25$, $\beta_N = 0.5$) and an ICRF-heated EDA H-mode shaped plasma ($\beta_p = 0.8$, $\beta_N = 1.0$). Both are at the same current, 600 kA, and toroidal field, 5.4 T. The $\alpha_z = 0$, $Z_{eff} = 1$ limits are assumed throughout.

The input profiles, shown in Figure 11, are similar to typical C-Mod shots and are converted into the coefficients used in Ref. 7, M_o^2, g and γg, assuming a molybdenum impurity, shown in Figure 12. Note that γg is used in the code to avoid a divide by zero error for flat profiles.

We start by verifying the output against the analytical theory for the centrifugal force only (A17) by artificially setting $g = 0$ in the code. The poloidal variation is plotted for the shaped plasma at $r/a \sim 0.5$ in Figure 13(a) and the radial profiles of the asymmetry are shown in Figure 13(b). The radial asymmetry profiles are calculated from $n(\theta)/n(0)$ by defining $[n_z(0) - n(\pi)]/[n_z(0) + n(\pi)]$ to be the in/out

asymmetry and $[n_z(\pi/2) - n(3\pi/2)]/[n_z(\pi/2) + n(3\pi/2)]$ to be the up/down asymmetry. In the $m = 1$ circular limit, these coefficients equal n_c and n_s, respectively. The code output, shown as the black solid line, matches the analytical result, red dashed-dotted line, very well and the $m = 1$ expansion, blue dashed line, has only a slight difference assumed to be due to shaping.

Next, the ion-impurity friction effects are added and the asymmetries are examined farther off axis at $r/a \sim 0.9$ and shown in Figure 1 in Sec. II. In this case, the asymmetry is not near either the strong rotation or strong ion-impurity friction, dotted green line, limits. The results are still in good agreement with the $m = 1$ expansion, and by running the
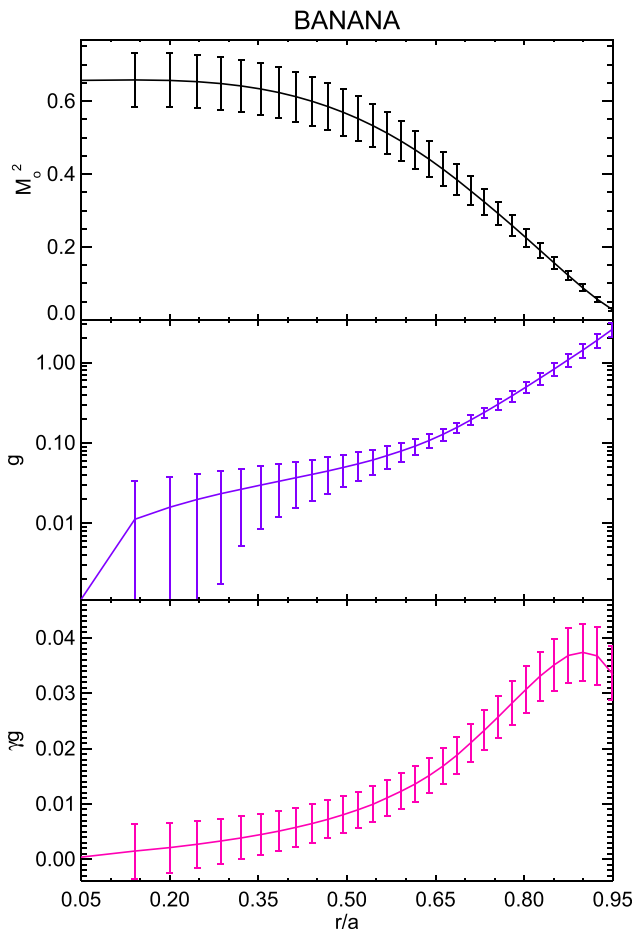

(a)

(b)

FIG. 13. Comparison of code against analytical limit assuming only toroidal rotation.

FIG. 12. Fülöp and Helander asymmetry parameters calculated from kinetic profiles for collisionless main-ions.

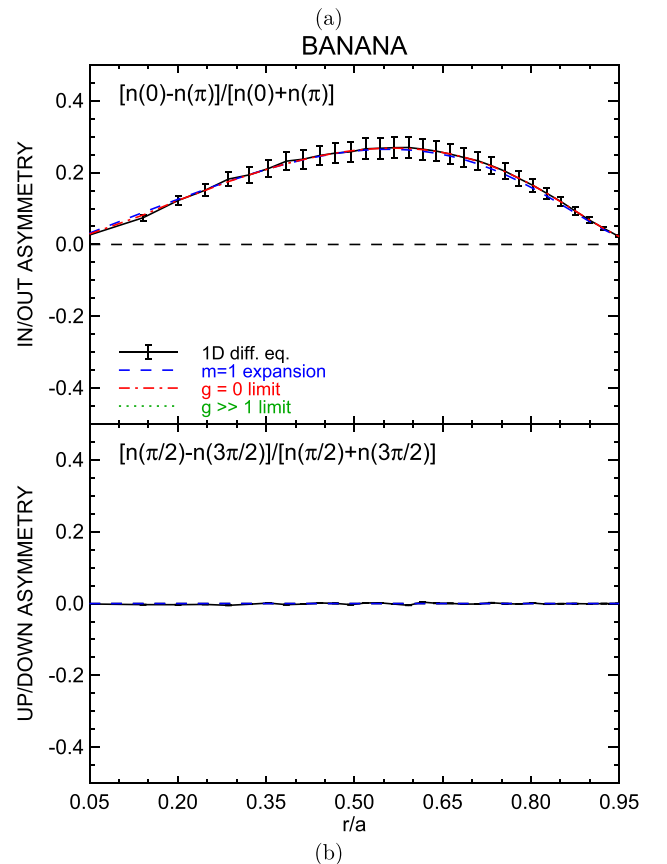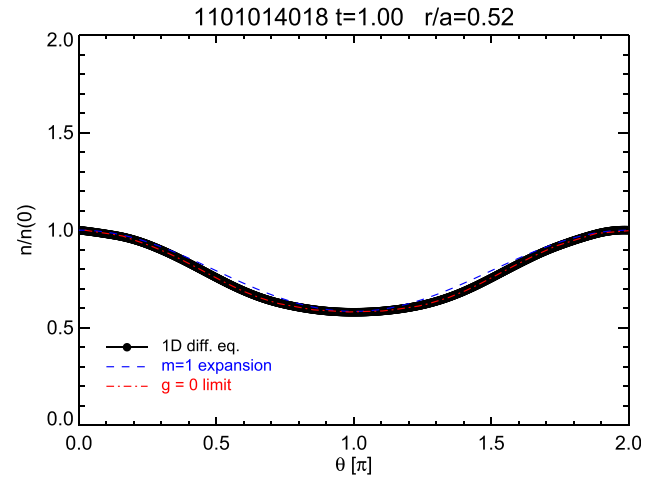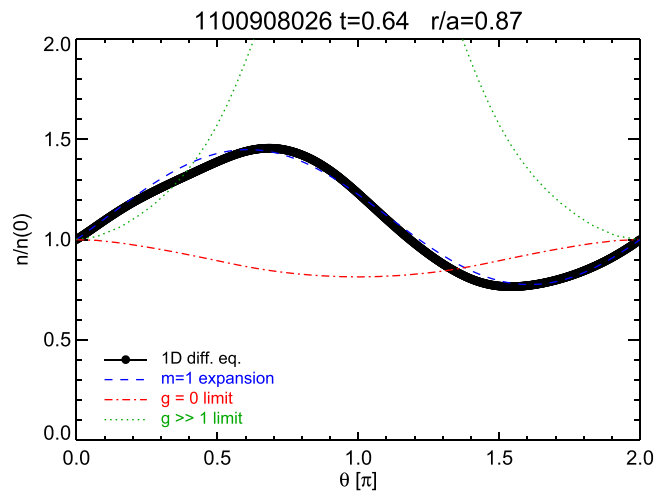FIG. 14. Repeat of analysis shown in Figure 13 using a circular plasma equilibrium.

same case using the circular equilibrium, shown in Figure 14, agreement between the code and the $m=1$ expansion is improved. This highlights that realistic plasma shaping has a small, but observable impact on the poloidal variation. Further verification of this code is provided in Ref. 16.

[1]S. K. Wong, Phys. Fluids **30**, 818 (1987).
[2]K. H. Burrell and S. K. Wong, Nucl. Fusion **19**, 1571 (1979).
[3]K. Brau, S. Suckewer, and S. K. Wong, Nucl. Fusion **23**, 1657 (1983).
[4]J. A. Wesson, Nucl. Fusion **37**, 577 (1997).
[5]P. Helander, Phys. Plasmas **5**, 1209 (1998).
[6]P. Helander, Phys. Plasmas **5**, 3999 (1998).
[7]T. Fülöp and P. Helander, Phys. Plasmas **6**, 3066 (1999).
[8]T. Fülöp and P. Helander, Phys. Plasmas **8**, 3305 (2001).
[9]M. Landreman, T. Fülöp, and D. Guszejnov, Phys. Plasmas **18**, 092507 (2011).
[10]M. L. Reinke *et al.*, Plasma Phys. Controlled Fusion **54**, 045004 (2012).
[11]A. Mollen *et al.*, Phys. Plasmas **19**, 052307 (2012).
[12]C. Angioni *et al.*, Phys. Plasmas **19**, 122311 (2012).
[13]L. C. Ingesson *et al.*, Plasma Phys. Controlled Fusion **42**, 161 (2000).
[14]P. Smeulders, Nucl. Fusion **26**, 267 (1986).
[15]H. Chen *et al.*, Phys. Plasmas **7**, 4567 (2000).
[16]M. L. Reinke, "Experimental tests of parallel impurity transport theory in tokamak plasmas," Ph.D. dissertation (Massachusetts Institute of Technology, 2011).
[17]P. Helander and D. J. Sigmar, *Collisional Transport in Magnetized Plasmas* (Cambridge University Press, 2002).
[18]N. T. Howard *et al.*, Phys. Plasmas **19**, 056110 (2012).
[19]M. L. Reinke *et al.*, Nucl. Fusion **53**, 043006 (2013).
[20]R. Dux *et al.*, Nucl. Fusion **39**, 1509 (1999).
[21]R. Giannella *et al.*, in *Proceedings of the 19th EPS Conference* (1992), Vol. 1, p. 279.
[22]B. Alper *et al.*, in *Proceedings of the 23rd EPS Conference* (1996), Vol. A, p. 051.
[23]L. C. Ingesson *et al.*, Nucl. Fusion **38**, 1675 (1998).
[24]M. Tendler, "Impurity transport in a rotating toroidal plasma with cold-gas mantle," in *Proceedings of the 8th Conference on Plasma Physics and Controlled Fusion* (1980), Vol. 1, p. 765.
[25]C. T. Hsu and D. J. Sigmar, Plasma Phys. Controlled Fusion **32**, 499 (1990).
[26]J. L. Terry *et al.*, Phys. Rev. Lett. **39**, 1615 (1977).
[27]S. Suckewer *et al.*, Technical Report No. PPPL-1430, Princeton Plasma Physics Lab, 1978.
[28]R. Durst, Nucl. Fusion **32**, 2238 (1992).
[29]K. W. Wenzel, "Measurements on injected impurity transport in TEXT (Texas Experimental Tokamak) using multiply filtered soft x-ray detectors," Ph.D. dissertation (Massachusetts Institute of Technology, 1990).
[30]S. P. Regan, "Soft X-ray spectroscopy on the Phaedrus-T tokamak," Ph.D. dissertation (Johns Hopkins University, 1996).
[31]W. Feneberg *et al.*, Technical Report No. JET-R(86)07, JET Joint Undertaking, 1986.
[32]J. E. Rice *et al.*, Nucl. Fusion **37**, 241 (1997).
[33]K. D. Marr *et al.*, Plasma Phys. Controlled Fusion **52**, 055010 (2010).
[34]R. M. Churchill *et al.*, "Inner-wall B^{5+} impurity density measurements using CXRS," in *52nd Annual Meeting of the APS Division of Plasma Physics, American Physical Society*, 2010.
[35]T. Pütterich *et al.*, Nucl. Fusion **52**, 083013 (2012).
[36]M. Romanelli and M. Ottaviani, Plasma Phys. Controlled Fusion **40**, 1767 (1998).
[37]K. H. Burrell, T. Ohkawa, and S. K. Wong, Phys. Rev. Lett. **47**, 511 (1981).
[38]W. Feneberg, Nucl. Fusion **29**, 1117 (1989).
[39]C. S. Chang and R. W. Harvey, Nucl. Fusion **23**, 935 (1983).
[40]N. P. Basse *et al.*, Fusion Sci. Technol. **51**, 476 (2007).
[41]A. Ince-Cushman *et al.*, Rev. Sci. Instrum. **79**, 10E302 (2008).
[42]M. L. Reinke *et al.*, Rev. Sci. Instrum. **83**, 113504 (2012).
[43]See http://www.ird-inc.com.
[44]M. L. Reinke and I. H. Hutchinson, Rev. Sci. Instrum. **79**, 10F306 (2008).
[45]A. W. Leonard *et al.*, Rev. Sci. Instrum. **66**, 1201 (1995).
[46]A. Huber *et al.*, Fusion Eng. Des. **82**, 1327 (2007).
[47]S. Konoshima *et al.*, Plasma Phys. Controlled Fusion **43**, 959 (2001).
[48]L. L. Lao *et al.*, Nucl. Fusion **25**, 1611 (1985).
[49]N. T. Howard *et al.*, Rev. Sci. Instrum. **82**, 033512 (2011).
[50]Ye. O. Kazakov *et al.*, Plasma Phys. Controlled Fusion **54**, 105010 (2012).
[51]J. W. Hughes *et al.*, Fusion Sci. Technol. **51**, 317 (2007).
[52]M. Greenwald *et al.*, Nucl. Fusion **47**, L26 (2007).
[53]Y. B. Kim *et al.*, Phys. Plasmas **3**, 2050 (1991).
[54]W. A. Houlberg, Phys. Plasmas **4**, 3230 (1997).
[55]E. A. Belli and J. Candy, Plasma Phys. Controlled Fusion **51**, 075018 (2009).
[56]R. A. Kolesnikov *et al.*, Phys. Plasmas **17**, 022506 (2010).
[57]B. A. Grierson *et al.*, Phys. Plasmas **19**, 056107 (2012).
[58]J. Kim *et al.*, Phys. Rev. Lett. **72**, 2199 (1994).
[59]K. Crombe *et al.*, Phys. Rev. Lett. **95**, 155003 (2005).
[60]W. M. Solomon *et al.*, Phys. Plasmas **13**, 056116 (2006).
[61]C. Chrystal *et al.*, Rev. Sci. Instrum. **83**, 10D501 (2012).
[62]A. Bortolon *et al.*, Nucl. Fusion **53**, 023002 (2013).